RSC Advances

ROYAL SOCIETY OF CHEMISTRY

PAPER

View Article Online
View Journal | View Issue

Check for updates

Cite this: *RSC Adv.*, 2023, **13**, 23700

Facile one-step hydrothermal synthesis of monolayer and turbostratic bilayer n-doped graphene quantum dots using sucrose as a carbon source†

Akkawat Ruammaitree, *[ab] Kanyaporn Praphanwong[a] and Arunocha Taiphol[a]

Received 1st July 2023
Accepted 26th July 2023

DOI: 10.1039/d3ra04402e

rsc.li/rsc-advances

Graphene quantum dots (GQDs) have attracted attention from researchers owing to their outstanding properties, such as chemical inertness, stable photoluminescence (PL), biocompatibility, and low toxicity, which make them suitable for bioimaging, optoelectronic device, sensor, and others. At present, there are several studies that report the effect of the size of GQDs on their properties; however, but there is only a few studies that report the effect of the thickness of GQDs on their properties. It may be attributed to the difficulty to obtain the accurate information on the thickness of GQDs. In this study, we demonstrate the facile and one-step hydrothermal synthesis of monolayer and bilayer n-doped graphene quantum dots (NGQDs) using sucrose as a carbon source. UV-visible and PL spectra show the quantum yield of the NGQDs is 4.9 times higher than that of the GQDs. Besides, the NGQDs exhibit sensitive PL for Ag^+ ions. In addition, the thickness distribution and interlayer spacing of NGQDs are revealed by X-ray diffraction (XRD) curve fitting, which is calculated using a simple and accurate equation. The information on the structure of the NGQDs from the XRD curve fitting is in a good agreement with the Raman results. This accurate estimation of the structure of GQDs by XRD curve fitting using the simple equation may extend the limits of GDQ study.

Introduction

Graphene is a two-dimensional layer that comprises carbon atoms arranged in a hexagonal honeycomb lattice. Graphene has no band gap due to a contact between valence and conduction bands at the Dirac point. However, the band gap of graphene appears when its lateral dimension reduces to less than 20 nm, which are known as graphene quantum dots (GQDs). GQDs have attracted attention from researchers owing to their outstanding properties, such as chemical inertness, stable photoluminescence (PL), biocompatibility, and low toxicity.[1] These make them suitable for bioimaging,[2] optoelectronic device,[3] sensor[4] and others. There are many studies on the synthesis of GQDs using various carbon sources, such as graphene oxide,[5] carbon fibers,[6] carbon black,[7] and glucose.[8] In 2022, Rocha *et al.* demonstrated the synthesis of GQDs using sucrose as a precursor of GQDs.[9] Although sucrose is cheap, widely available, and non-toxic saccharide, the synthesis method of GDQs by Rocha *et al.* has many steps leading to the production of GQDs quite complicates. Besides, many reports revealed that nitrogen doping can enhance the PL intensity of GQDs, *e.g.* Santiago *et al.* synthesized nitrogen-doped GQDs (NGQDs) by irradiating graphene oxide and urea solution using an optical parametric oscillator.[10] However, this method is not convenient for common laboratory because the optical parametric oscillator is not a common instrument. In addition, the preparation of graphene oxide has many steps and is time consuming. Moreover, this method is not suitable for large scale production with low cost. Hydrothermal synthesis is a general method that is widely used to synthesize single crystals owing to the facile, low-cost, and scalable production. Thus, the hydrothermal method is suitable for large scale production of NGQDs with low cost.

Recently, there are several studies on the effect of the size of GQDs on their properties (such as PL);[11] however, only a few studies are there on the effect of the thickness of GQDs on their properties. It may be attributed to the lack of facile and accurate method for estimating the thickness and stacking structure of GQDs. Although there are researchers studying the properties of bilayer GQDs, which are fabricated from bilayer graphene using Raman spectroscopy measurements to clearly identify the bilayer graphene,[12] the Raman spectroscopy can unambiguously clarify only AB-stacked bilayer graphene. Therefore, in order to extend the limit of the GDQ study, a simple and

---

[a] *Department of Physics, Faculty of Science and Technology, Thammasat University, Pathum Thani 12120, Thailand. E-mail: akkawat@tu.ac.th*

[b] *Thammasat University Research Unit in Synthesis and Applications of Graphene, Thammasat University, Pathum Thani 12120, Thailand*

† Electronic supplementary information (ESI) available. See DOI: https://doi.org/10.1039/d3ra04402e

accurate method for estimating the thickness and stacking structure of GQDs is needed. X-ray diffraction (XRD) is a common technique for studying the structure of a material. However, many researchers obtained only the rough interlayer spacing of GQDs by analysing the graphene peak position of XRD pattern.[13]

In this study, we demonstrate a facile and one-step hydrothermal synthesis of monolayer and turbostratic bilayer NGQDs using sucrose as a carbon source. The structure of NGQDs is revealed by XRD curve fitting, which is calculated using a simple and accurate equation. The information on the structure of the NGQDs from the XRD curve fitting is confirmed by the Raman results. The optical properties of NGQDs are investigated using UV-visible absorbance and PL emission spectroscopies. The nitrogen doping is confirmed using X-ray photoelectron spectroscopy (XPS) and Fourier transform infrared (FTIR) spectroscopy. The PL on–off–on switching behavior of NGQDs for Ag^+ ions is also studied.

Materials and methods

Synthesis of NGQDs

1 g sucrose and 2 mL ethylenediamine were dissolved in 50 mL deionized water. The solution was sonicated for 30 min followed by stirring for 20 min. After that, the solution was transferred into a Teflon-lined stainless-steel autoclave and heated at 170 °C for 7 h. Then, the sample was naturally cooled down to room temperature. Thereafter, the solution was filtered for 2 days by dialysis using MW500 dialysis bag to obtain NGQDs. For comparison, the GQDs were synthesized by the same process without the addition of ethylenediamine.

Characterization

UV-visible spectra and PL spectra were recorded using a Duetta, Horiba Scientific instrument at room temperature. The PL lifetime measurements were carried out using a FluoroMax Plus spectrofluorometer, Horiba Scientific at room temperature with excitation at 369 nm. XRD was performed on benchtop X-ray powder diffractometer (Bruker) using Cu-Kα radiation ($\lambda = 0.154184$ nm). Raman spectra were measured using a Horiba instrument at room temperature using the laser wavelength and spot size of 532 nm and ~1 μm, respectively. XPS was measured by Axis Supra, Kratos under the base pressure of $\sim 2 \times 10^{-9}$ Torr. Transmission electron microscopy (TEM) images were acquired using a Hitachi HT7800, operating at an accelerating voltage of 80 kV. FTIR spectroscopy was carried out using a Shimadzu IRTracer-100 at room temperature.

Results and discussion

The optical properties of NGQDs and GQDs in aqueous solution were investigated using UV-visible absorbance and PL emission spectroscopy, as shown in Fig. 1. Fig. 1(a) displays the UV-visible spectra of the NGQDs and GQDs in the range from 200 nm to 700 nm. The UV-visible spectra of the GQDs showed a strong absorption in the UV range while the light absorbance of the NGQDs was broader and extended further to ~500 nm, which is in the visible range revealing that the nitrogen doping can narrow the bandgap of NGQDs.[14] The UV-visible spectra of the NGQDs and GQDs displayed an absorption band at ~230 nm, which corresponds to the π–π* excitation of the π-bonds.[15] In addition, GQDs exhibited an extremely strong light absorbance at 284 nm, which was much higher than that of NGQDs. This strong absorption results from the π–π* transition, which is characteristic for GQDs.[1] The absorption shoulder of NGQDs at ~370 nm arises from the n–π* transition. It much red shifted from general GQDs (~300 nm). Fig. 1(b) and (c) show the PL spectra of the NGQDs and GQDs, respectively, with various excitations wavelength revealing the emission peak positions red shifts when the excitation wavelength increases from 360 nm to 500 nm. The redshift of the emission peak positions reveals that the size and emissive site of the NGQDs and GQDs are not uniform.[16] Fig. S1† displays a photograph of NGQDs prepared by hydrothermal process at 130 to 210 °C. The color of NGQD solution changed from yellow to brown when the temperature increases, indicating the concentration of NGQDs increased with the temperature. In addition, the quantum yield of GQDs can be calculated using the following equation

$$\Phi_x = \Phi_{st}(K_x/K_{st})(\eta_x/\eta_{st}) \tag{1}$$

where Φ, K_x, and η are quantum yield, the slope of the graph between the PL intensity and UV-visible intensity, and the refractive index of the solvent, respectively. st and x refer to standard and unknown samples, respectively. Fig. 1(d) presents slopes of graph between the integrated fluorescence intensity and UV absorbance of NGQDs and GQDs are 3169 and 648, respectively, implying that the quantum yield of NGQDs is 4.9 times higher than that of GQDs. Fig. S2† shows the slopes of graph between the integrated fluorescence intensity and UV absorbance of NGQD solution prepared by hydrothermal process at 130 to 210 °C, revealing the slope and yield depended on the temperature (Table S1†).

Fig. 1(e) displays the PL stability of NGQDs and GQDs under continuous 360 nm excitation wavelength for 1 h. The intensities of NGQDs and GQDs were decreased by 13.52% and 2.44%, respectively. Although the photobleaching of NGQDs was obviously higher than that of GQDs, the synthesized NGQDs were more stable than Xiong *et al.*'s NQGDs ($e\text{-GQDs}_{200}$), which were synthesized by hydrothermal procedure using monolayer graphene oxide sheets as a carbon source.[17] The intensity of $e\text{-GQDs}_{200}$ was decreased by more than 40% after 1 h of exposure. Xiong *et al.* reported that the strong photobleaching of NQGDs was due to the oxidative destruction of the N-doping sites. Cheng Cheng *et al.* found that the PL lifetime of quantum dots decreased when the particle size increased.[18] Fig. 1(f) shows the PL decays of NGQDs and GQDs. The PL lifetimes of the NGQDs and GQDs were 3.60 and 2.68 ns, respectively, indicating the size of NGQDs was smaller than that of GQDs.

Fig. 2(a) displays the XRD pattern and the fitting curve of the NGQDs. The fitting curve was calculated using the following equation[19]

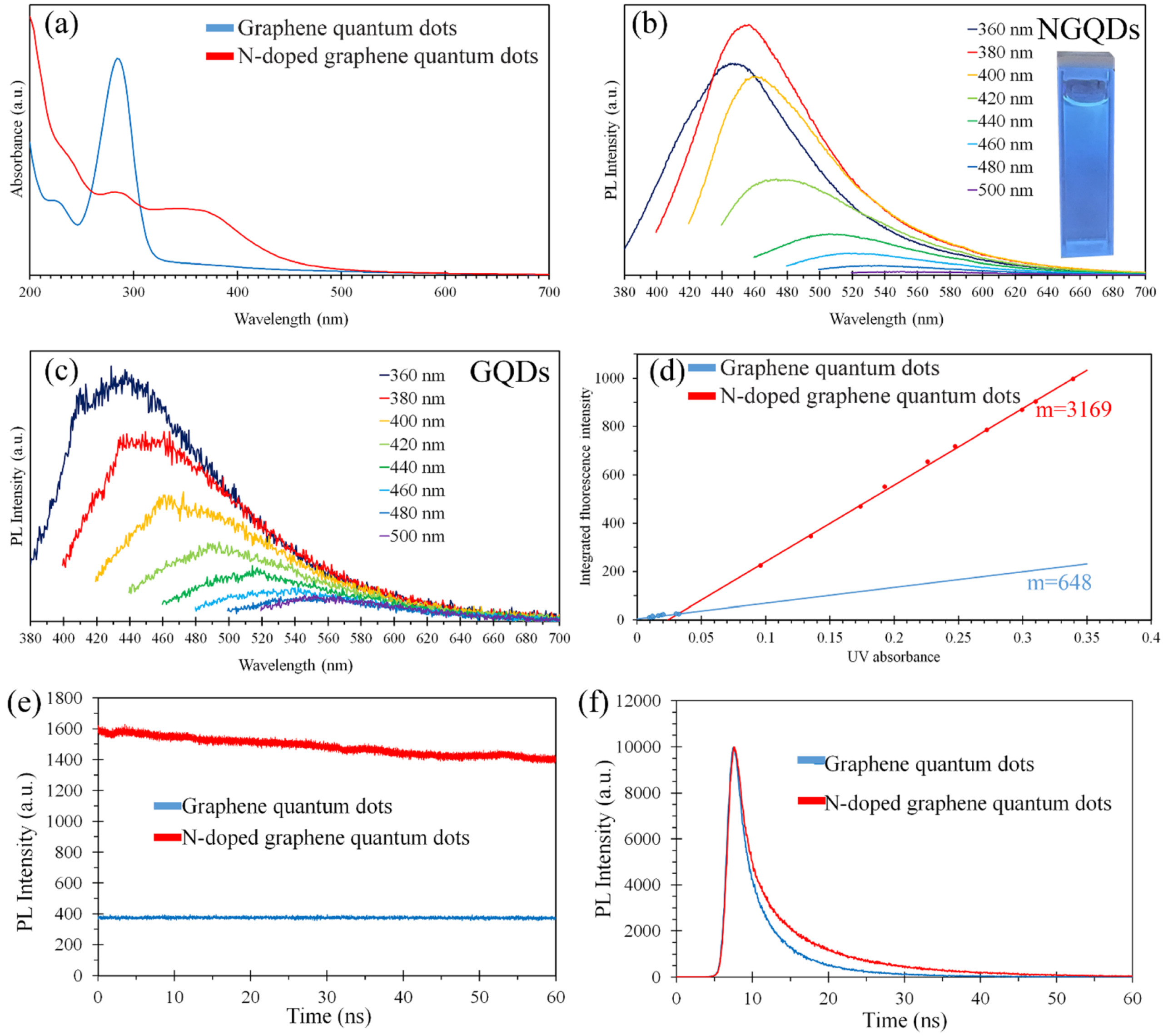

Fig. 1 (a) UV-visible spectra of NGQDs (red) and GQDs (blue). (b) and (c) PL spectra of NGQDs and GQDs (respectively) with various excitation wavelength. Inset of (b) photograph of the NGQD solution emitting blue PL under a handheld 365 nm UV light. (d) Relationship between the integrated fluorescence intensity and UV absorbance of NGQDs (red) and GQDs (blue) using the excitation wavelength of 360 nm. (e) The photobleaching performance of the NGQD and GQD solutions under continuous excitation and emission wavelengths of 360 and 450 nm, respectively, for 1 h. (f) PL decays of NGQDs and GQDs.

$$I \propto |f(\theta)|^2 \left| \sum_{j=0}^{N-1} \beta_j e^{ika_j j} \right|^2 \tag{2}$$

where I is XRD intensity, $f(\theta)$ is the atomic scattering of carbon,[20] N is the layer number of graphene, and β_j is the occupancy of $(j+1)^{\text{th}}$ graphene layer. $ka_j = (4\pi d_j \sin\theta)/\lambda$ where d_j is the interlayer spacing of graphene, θ is an incident angle, and λ is the wavelength of incident X-ray beam. Fig. 2(a) inset shows the fitting parameters of the calculation curve. The chi-squared (χ^2) dependence of the fitting parameters (Fig. S3†) indicated a good fit between the calculation curve and experimental XRD data, revealing that the NGQDs contained 74% monolayer graphene and 26% bilayer graphene (Fig. 2(b)). The interlayer spacing of bilayer graphene was 3.5 Å, which was much wider than that of AB stacked graphene (3.35 Å), implying that the stacking structure of the bilayer graphene in the NGQDs was turbostratic stacking.

Fig. 2(c) shows the Raman spectra of GQDs and the NGQDs. For GQDs, the Raman spectrum displayed the graphene characteristic peaks of D, G, and 2D bands at 1352 cm^{-1}, 1548 cm^{-1}, and 2656 cm^{-1}, respectively. D, G, and 2D bands originate from the breathing modes of six-atom rings,[21] E_{2g} vibrational mode, and second-order two-phonon mode, respectively.[22] In general, the large area graphene contains the 2D band at ~2700 cm^{-1},[23] whereas the position of the 2D band of GQDs showed a red shift of ~45 cm^{-1}. In addition, the peak intensity ratio of G band to 2D band (I_G/I_{2D}) was more than one. It is different from the

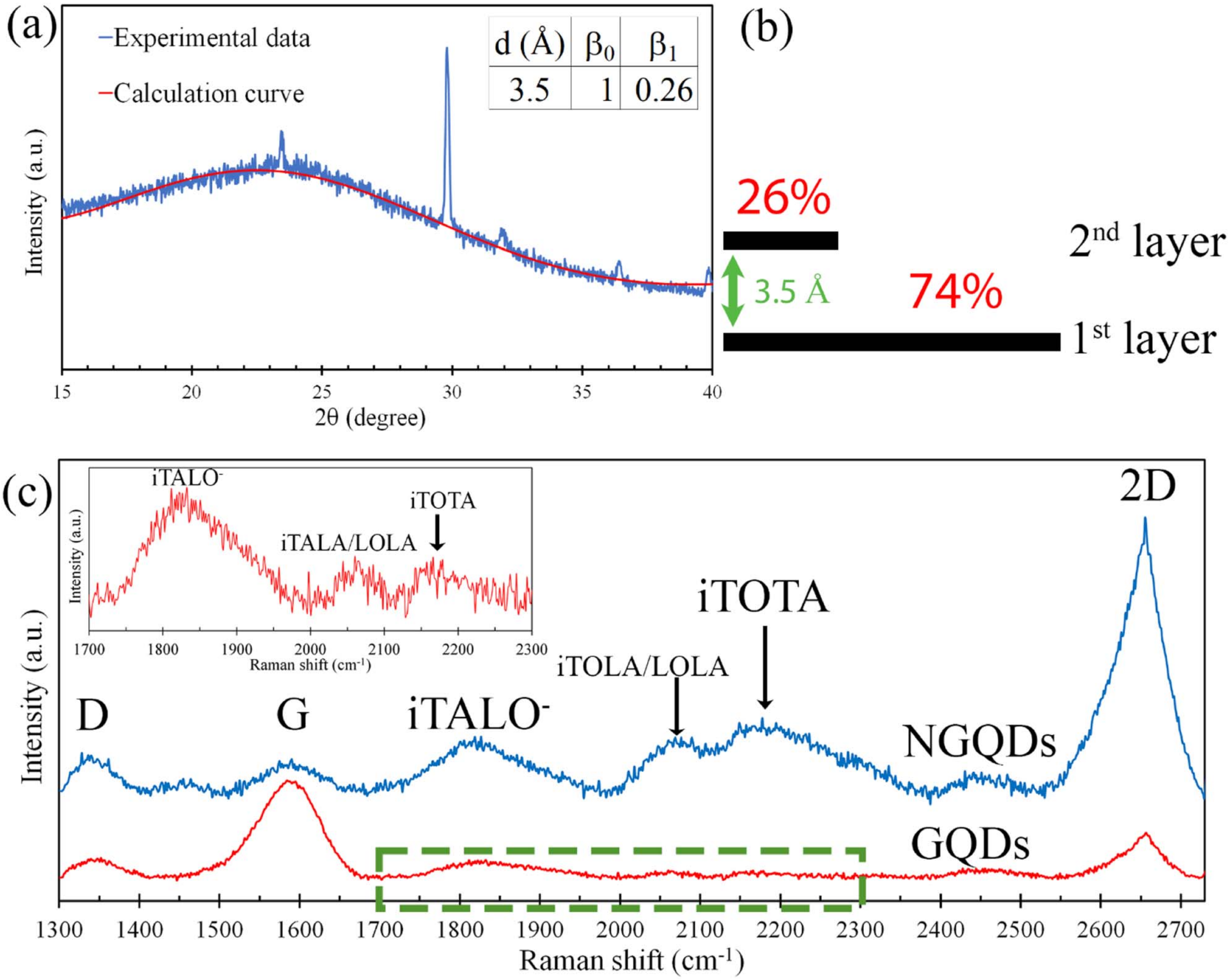

Fig. 2 (a) Experimental (blue) and calculation (red) XRD pattern of the NGQDs. (b) Schematic of the structure of NGQDs. (c) Raman spectra of GQDs (red) and NGQDs (blue). Inset magnified Raman spectrum of GQDs.

general large area monolayer graphene, which contains the I_G/I_{2D} less than one.[24] However, the red-shift of 2D band and the I_G/I_{2D} corresponded to those of GQDs, which were synthesized *via* standard solution-based methods and displayed the peak position of 2D band at 2614 cm^{-1} and the I_G/I_{2D} more than one.[25] In the case of the NGQDs, the I_G/I_{2D} was less than one. It is corresponding to monolayer nitrogen-doped graphene sheets synthesised by chemical vapor deposition process with pyridine as the sole source of both carbon and nitrogen.[26] Nowadays, I_G/I_{2D} is widely utilized to estimate the graphene thickness.[27] However, several studies reported that I_G/I_{2D} also depends on the doping.[28] Moreover, this study showed that I_G/I_{2D} depends on the graphene size as well. Therefore, the estimation of graphene thickness using only I_G/I_{2D} may be not accurate.

The intensity ratio of D band to G band (I_D/I_G) is widely used to estimate the grain size of graphene (L_a) using the following equation[29]

$$L_a\ (\text{nm}) = (2.4 \times 10^{-10})\ \lambda^4\ (I_D/I_G)^{-1} \tag{3}$$

where λ is the wavelength of the incident laser in nanometer unit. The I_D/I_G of GQDs and NGQDs were 0.194 and 1.148, respectively, resulting in the graphene grain sizes of GQDs and NGQDs to be 98.9 nm and 16.7 nm, respectively. Liu *et al.* observed that the PL and quantum yield increase when the graphene size decreases.[30] The Raman results, which showed the size of NGQDs is ~6 times smaller than that of GQDs, corresponded to the UV-visible and PL results that showed the quantum yield of NGQDs was 4.9 times higher than that of GQDs.

Fig. 2(c) inset displays the magnified Raman spectrum of GQDs in the range from 1700 cm^{-1} to 2300 cm^{-1}, exhibiting 3 weak intensity peaks at 1833 cm^{-1} (iTALO$^-$), 2065 cm^{-1} (iTALA/LOLA), and 2157 cm^{-1} (iTOTA). The iTALO$^-$ mode originates from the combination of in-plane transverse acoustic (iTA) and longitudinal optic (LO) phonons. Rao *et al.* reported that the peak intensity of the iTALO$^-$ mode is high for single layer graphene and turbostratic graphene, but it rapidly reduces with the increment of the layer number of AB stacked graphene.[31] They also showed that the peak intensity of the iTALO$^-$ mode is

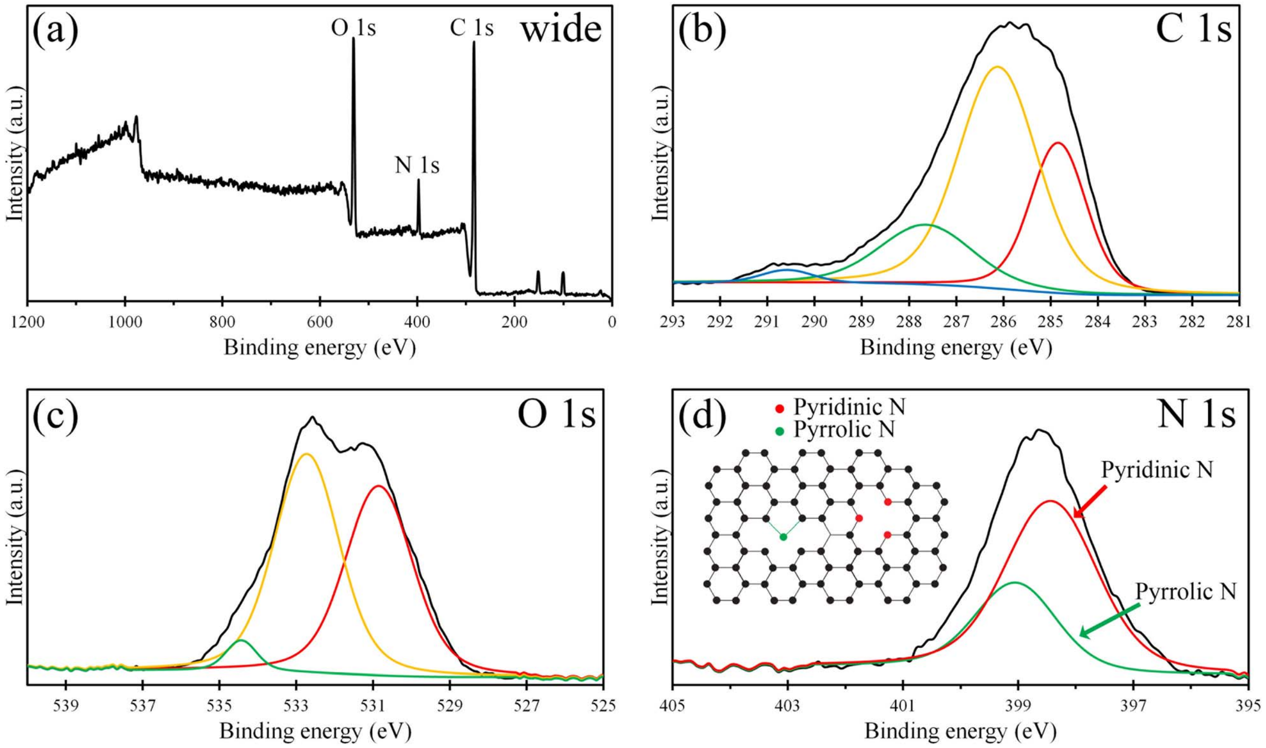

Fig. 3 (a) Wide-scan, (b) C 1s, (c) O 1s, and (d) N 1s XPS spectra of the NGQDs. (d) Inset schematic of N configuration of NGQDs.

considerably low in the case of AB-stacked few-layer graphene and disappears in the case of thick highly ordered pyrolytic graphite (HOPG). However, in the case of NGQDs, the intensities of iTALO$^-$, iTALA/LOLA, and iTOTA modes were obviously higher than that of GQDs. The appearance of the high intensity of iTALO$^-$ mode confirmed the presence of single layer graphene and turbostratic graphene in NGQDs. It is in good agreement with the XRD results, which revealed that NGQDs contained 74% monolayer graphene and 26% turbostratic bilayer graphene.

M band is an overtone of the out-of-plane transverse optical phonon mode and commonly observed at ~1750 cm^{-1} in AB stacked bilayer graphene or few layer graphene or graphite.[31,32] The M band arises from the strong interlayer interaction between the graphene layers. Thus, the M band vanishes in the case of monolayer graphene and turbostratic graphene due to a lack of interlayer interaction. The absence of M band in the Raman spectrum of NGQDs is corresponding with the XRD results, revealing that the interlayer spacing of NGQDs is much wider than that of AB stacked graphene.

M$^-$ band is the lower frequency peak in the M band and generally appears at ~1730 cm^{-1}.[31–33] It is commonly present with the iTALO$^-$ mode in the case of AB-stacked bilayer graphene. Hence, the disappearance of M$^-$ band confirmed that there is no AB-stacked bilayer graphene in NGQDs. It is in a good agreement with the XRD results, which indicated that the stacking structure of bilayer graphene in NGQDs is turbostratic stacking.

Nowadays, the turbostratic graphene can be synthesized by various methods, such as chemical vapor deposition,[34] physical vapor deposition,[35] negative carbon ion implantation,[36] laser-assisted process,[37] flash Joule heating process,[38] solar radiation,[40] and calcination.[41] However, factors that effect on the growth of turbostratic graphene are still unclear. In 2021, Athanasiou *et al.* stated that the main factors for the growth of turbostratic graphene were the fast heating and cooling rates.[37] In 2023, our previous study showed that the main factor of the growth of turbostratic graphene was the fast cooling rate only.[41] However, the results in this report confirmed that the high pressure is also a key factor for the formation of turbostratic graphene.

Fig. 3(a) shows the XPS survey spectrum of NGQDs displaying 3 significant peaks of the C 1s, N 1s, and O 1s at ~283 eV, 397 eV, and 531 eV with the atomic concentration of 50.34%, 6.92%, and 42.74%, respectively. For the C 1s XPS spectrum (Fig. 3(b)), the deconvolution shows 4 peaks of C–C, C–OH, C=O/C–N, and COOH at 284.8 eV, 286.1 eV, 287.6 eV, and 290.6 eV, respectively, indicating the presence of graphitic carbon, carboxyl functional groups, and N doping. The C–N peak overlaid the C=O peak around the binding energy of 287.5 ± 0.5 eV.[39] Fig. 3(c) presents the O 1s XPS spectrum, which was deconvoluted into 3 peaks at 530.85 eV, 532.72 eV, and 534.43 eV, which correspond to COOH, C=O, and C–OH, respectively. The incorporation of N in the graphene structure was revealed by deconvoluting the N 1s XPS spectrum (Fig. 3(d)). The deconvolution exhibits 2 peaks at 398.4 eV and 399.0 eV, which are corresponding to pyridinic and pyrrolic C–N

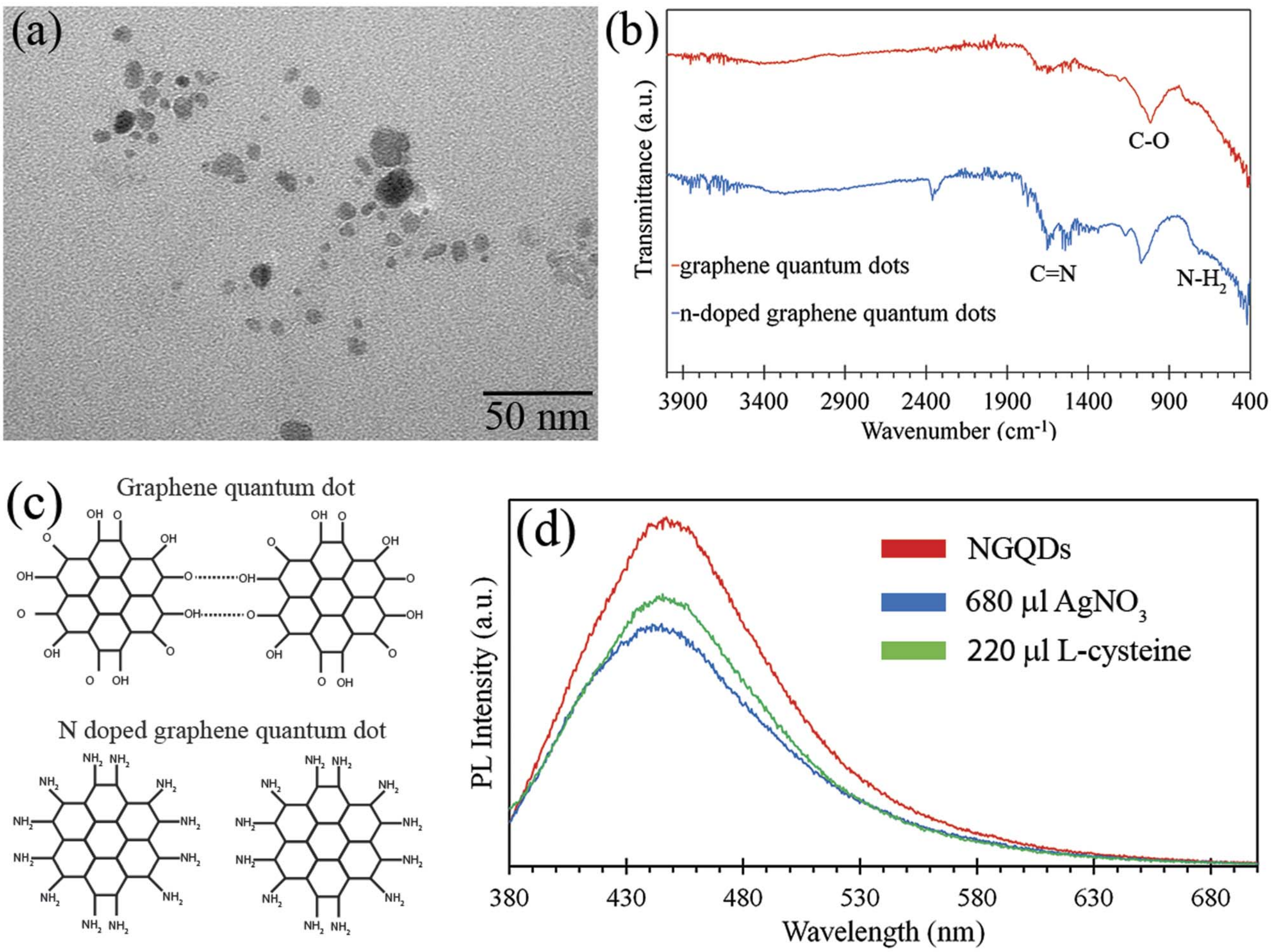

Fig. 4 (a) TEM image of the NGQDs. (b) FTIR spectra of the NGQDs (blue) and the GQDs (red). (c) Schematic of GQDs aggregation and NGQDs separation. (d) PL spectra of NGQDs (red), NGQDs after adding $AgNO_3$ solution (blue), and NGQDs after adding $AgNO_3$ and cysteine solution (green).

configurations, respectively. The concentration of pyridinic N and pyrrolic N were 69.1% and 30.9%, respectively. Fig. 3(d) inset shows a schematic of C–N configuration of NGQDs. In the case of the pyridinic N, a nitrogen atom is bonded with two carbon atoms by the sp^2 hybridized bonding. For pyrrolic N, a nitrogen atom replaces the carbon atoms in the hexagonal graphene lattice and forms the sp^3 hybridized bonding in the five-atom ring. However, the peak of graphitic N was absent. It is different from n-doped graphene, which was synthesized by nitrogen plasma treatment[39] and n-doped graphene quantum dots synthesized by pulsed laser ablation[10] which contain graphitic C–N configuration.

Fig. 4(a) displays a TEM image of NGQDs showing the size of NGQDs was in the range of 3–20 nm. It is in a good agreement with Raman results, which revealed that the size of NGQDs was 16.7 nm. In addition, it corresponds to the shift of PL in Fig. 1(b), which implied that the size of NGQDs was not uniform. Fig. 4(b) displays the FTIR spectra of GQDs and NGQDs. Both GQDs and NGQDs contained a C–O peak at 1014 cm^{-1} and 1074 cm^{-1}, respectively. The FTIR spectrum of NGQDs also shows the peaks of the bending vibrations of $N–H_2$ bonds at 716 cm^{-1} and stretching vibration of C=N bonds at 1683 cm^{-1},[42] confirming the nitrogen doping on the surface and the presence of amine functional groups at the edge of the NGQDs.

The Raman results revealed that the size of NGQDs was much smaller than that of GQDs. In addition, the PL results of NGQDs and GQDs (Fig. 1) showed that the emission peak intensity and quantum yield of NGQDs were much higher than those of GQDs, implying that the size of NGQDs was smaller than that of GQDs. Fig. 4(c) illustrates the aggregation of GQDs and the separated NGQDs. For GQDs, there were hydroxyl and carbonyl groups attached to the edge of GQDs. The GQDs aggregated due to the intermolecular H-bonding between the carboxylic groups at the edge of GQDs.[43] On the other hand, there was no intermolecular H-bonding in the case of NGQDs due to the attachment of amines at the edge, resulting in the separation of NGQDs. These results corresponded to the amine-terminated GQDs (Am-GQDs), which were synthesized by Suryawanshi *et al.*[43]

Suryawanshi *et al.* demonstrated the PL on–off–on switching behavior of Am-GQDs for Ag^+ ions.[43] The PL intensity of Am-

GQDs decreased when the Am-GQDs detected Ag^+ ions and it rebounded after subsequent the addition of L-cysteine. Fig. 4(d) shows the PL spectra of NGQDs before and after adding 680 μL of $AgNO_3$ (3 mM) and 220 μL of L-cysteine (3 mM) solution. It was obviously observed that the PL emission intensity reduced after NGQDs detected the Ag^+ ions. However, the PL emission intensity was regenerated after subsequent addition of 220 μL L-cysteine solution. Fig. S4† shows the PL on–off–on mechanism of NGQDs for Ag^+ ions. After the addition of $AgNO_3$, Ag was bonded with the amines at the edge of NGQDs, resulting in the decrease in the PL intensity because the excited electron was transferred from the LUMO of NGQDs to Ag^+ ions. However, the PL intensity of NGQDs was regenerated after removing the Ag^+ ions by the addition of L-cysteine. This is in good agreement with Am-GQDs from Suryawanshi *et al.*, indicating that NGQDs can serve as sensors for Ag^+ ions. Although both of Am-GQDs from Suryawanshi *et al.* and our NGQDs are specific to the Ag^+ ions, the production of our NGQDs is much simpler.

Conclusions

We have demonstrated the facile and one-step hydrothermal synthesis of monolayer and turbostratic bilayer n-doped graphene quantum dot using sucrose as a carbon source. The UV-visible and PL spectra showed the quantum yield of NGQDs was obviously higher than that of GQDs. Besides, NGQDs exhibited sensitive PL for Ag^+ ions. In addition, the structure of NGQDs, such as the thickness distribution and interlayer spacing, was revealed by XRD curve fitting, which was calculated using the simple and accurate equation. The information on the structure of NGQDs from the XRD results is in a good agreement with the Raman results. We hope that this accurate estimation of the structure of GQDs by XRD curve fitting using the simple equation could extend the limit of GDQ study.

Conflicts of interest

There are no conflicts to declare.

Acknowledgements

This work was supported by the Thailand Science Research and Innovation Fundamental Fund fiscal year 2023, and Thammasat University Research Fund, Contract No. TUFT 7/2564, and Thammasat University Research Unit in Synthesis and Applications of Graphene.

Notes and references

1 M. Shehab, S. Ebrahim and M. Soliman, *J. Lumin.*, 2017, **184**, 110.

2 S. Zhu, J. Zhang, C. Qiao, S. Tang, Y. Li, W. Yuan, B. Li, L. Tian, F. Liu, R. Hu, H. Gao, H. Wei, H. Zhang, H. Sunb and B. Yang, *Chem. Commun.*, 2011, **47**, 6858.

3 O. Salihoglu, N. Kakenov, O. Balci, S. Balci and C. Kocabas, *ACS Photonics*, 2018, **5**, 2384.

4 Y. Dong, G. Li, N. Zhou, R. Wang, Y. Chi and G. Chen, *Anal. Chem.*, 2012, **84**, 8378.

5 D. Du, K. Wang, Y. Wen, Y. Li and Y. Y. Li, *ACS Appl. Mater. Interfaces*, 2016, **8**, 3287.

6 Y. Song and S. Chen, *ACS Appl. Mater. Interfaces*, 2014, **6**, 14050.

7 L. Chen, C. X. Guo, Q. Zhang, Y. Lei, J. Xie, S. Ee, G. Guai, Q. Song and C. M. Li, *ACS Appl. Mater. Interfaces*, 2013, **5**, 2047.

8 Y. J. Lee, T. W. Yeh, C. Zou, Z. P. Yang, J. W. Chen, P. L. Hsu, J. L. Shen, C. C. Chang, J. K. Sheu and L. Y. Lin, *ACS Photonics*, 2019, **6**, 2894.

9 A. P. M. Rocha, M. I. Alayo and D. M. Silva, *Appl. Sci.*, 2022, **12**, 8686.

10 S. R. M. Santiago, Y. A. Wong, T. N. Lin, C. H. Chang, C. T. Yuan and J. L. Shen, *Opt. Lett.*, 2017, **42**, 3642.

11 F. Zhang, F. Liu, C. Wang, X. Xin, J. Liu, S. Guo and J. Zhang, *ACS Appl. Mater. Interfaces*, 2016, **8**, 2104.

12 C. Volk, S. Fringes, B. Terres, J. Dauber, S. Engels, S. Trellenkamp and C. Stampfer, *Nano Lett.*, 2011, **11**, 3581; M. Wang, E. B. Song, S. Lee, J. Tang, M. Lang, C. Zeng, G. Xu, Y. Zhou and K. L. Wang, *ACS Nano*, 2011, **5**, 8769.

13 Y. K. Lv, Y. Y. Li, R. H. Zhou, Y. P. Pan, H. C. Yao and Z. J. Li, *ACS Appl. Mater. Interfaces*, 2020, **12**, 34245; T. Selvakumar, M. Rajaram, A. Natarajan, L. Harikrishnan, K. Alwar and A. Rajaram, *ACS Omega*, 2022, **7**, 12825; S. Reagen, Y. Wu, R. Shahni, W. Sun, J. Zhang, Q. R. Chu, X. Hou, C. Combs and J. X. Zhao, *ACS Omega*, 2022, **7**, 38902.

14 Y. Yan, J. Chen, N. Li, J. Tian, K. Li, J. Jiang, J. Liu, Q. Tian and P. Chen, *ACS Nano*, 2018, **12**, 3523.

15 M. Bacon, S. J. Bradley and T. Nann, *Part. Part. Syst. Charact.*, 2014, **31**, 415.

16 J. Gu, M. J. Hu, Q. Q. Guo, Z. F. Ding, X. L. Sun and J. Yang, *RSC Adv.*, 2014, **4**, 50141; M. Kaur, S. K. Mehta and S. K. Kansal, *Sens. Actuators, B*, 2017, **245**, 938; M. Kaur, S. K Mehta and S. K. Kansal, *Spectrochim. Acta, Part A*, 2017, **180**, 37; L. Li, L. Li, C. Wang, K. Liu, R. Zhu, H. Qiang and Y. Lin, *Microchim. Acta*, 2015, **182**, 763; X. Liu, W. Gao, X. Zhou and Y. Ma, *J. Mater. Res.*, 2014, **29**, 1401.

17 Y. Xiong, J. Schneider, C. J. Reckmeier, H. Huang, P. Kasákb and A. L. Rogach, *Nanoscale*, 2017, **9**, 11730.

18 C. Cheng, J. Lia and X. Cheng, *J. Lumin.*, 2017, **188**, 252.

19 A. Ruammaitree, H. Nakahara, K. Akimoto, K. Soda and Y. Saito, *Applied Surface Science*, 2013, **282**, 297; P. Surinlert, P. Kokmat and A. Ruammaitree, *RSC Adv.*, 2022, **12**, 25048.

20 P. Brown, A. Fox, E. Maslen, M. O. Keefe and B. Willis, *International Tables for Crystallography C*, 2004, **6**, 555.

21 A. C. Ferrari and D. M. Basko, *Nat. Nanotechnol.*, 2013, **8**, 235.

22 M. J. Allen, V. C. Tung and R. B. Kaner, *Chem. Rev.*, 2010, **110**, 132.

23 P. Surinlert and A. Ruammaitree, *Solid State Phenom.*, 2020, **302**, 79; P. Kokmat, N. Donnuea, N. Nuntawong, A. Wisitsoraat and A. Ruammaitree, *IOP Conf. Ser.: Mater. Sci. Eng.*, 2019, **526**, 012008.

24 Y. Y. Wang, Z. H. Ni, T. Yu, Z. X. Shen, H. M. Wang, Y. H. Wu, W. Chen and A. T. S. Wee, *J. Phys. Chem. C*, 2008, **112**, 10637.
25 E. Dervishi, Z. Ji, H. Htoon, M. Sykora and S. K. Doorn, *Nanoscale*, 2019, **11**, 16571.
26 Z. Jin, J. Yao, C. Kittrell and J. M. Tour, *ACS Nano*, 2011, **5**, 4112.
27 Y. Hwangbo, C. Lee, A. E. Mag-Isa, J. Jang, H. Lee, S. Lee, S. Kim and J. Kim, *Carbon*, 2014, **77**, 454.
28 A. Das, S. Pisana, B. Chakraborty, S. Piscanec, S. K. Saha, U. V. Waghmare, K. S. Novoselov, H. R. Krishnamurthy, A. K. Geim, A. C. Ferrari and A. K. Sood, *Nat. Nanotechnol.*, 2008, **3**, 210.
29 M. A. Pimenta, G. Dresselhaus, M. S. Dresselhaus, L. G. Cancado, A. Jorio and R. Saito, *Phys. Chem. Chem. Phys.*, 2007, **9**, 1276.
30 Z. Liu, F. Li, Y. Luo, M. Li, G. Hu, X. Pu, T. Tang, J. Wen, X. Li and W. Li, *Molecules*, 2021, **26**, 3922.
31 R. Rao, R. Podila, R. Tsuchikawa, J. Katoch, D. Tishler, A. M. Rao and M. Ishigami, *ACS Nano*, 2011, **5**, 1594.
32 C. Cong, T. Yu, R. Saito, G. F. Dresselhaus and M. S. Dresselhaus, *ACS Nano*, 2011, **5**, 1600.
33 V. W. Brar, Ge. G. Samsonidze, M. S. Dresselhaus, G. Dresselhaus, R. Saito, A. K. Swan, M. S. Unlu, B. B. Goldberg, A. G. Souza Filho and A. Jorio, *Phys. Rev. B: Condens. Matter Mater. Phys.*, 2002, **66**, 155418.
34 C. Wei, R. Negishi, Y. Ogawa, M. Akabori, Y. Taniyasu and Y. Kobayashi, *Jpn. J. Appl. Phys.*, 2019, **58**, SIIB04.
35 J. A. Garlow, L. K. Barrett, L. Wu, K. Kisslinger, Y. Zhu and J. F. Pulecio, *Sci. Rep.*, 2016, **6**, 19804.
36 K. Liu, F. Lu, K. Li, Y. Xu and C. Ma, *Appl. Surf. Sci.*, 2019, **493**, 1255.
37 M. Athanasiou, N. Samartzis, L. Sygellou, V. Dracopoulos, T. Ioannides and S. N. Yannopoulos, *Carbon*, 2021, **172**, 750.
38 K. M. Wyss, Z. Wang, L. B. Alemany, C. Kittrell and J. M. Tour, *ACS Nano*, 2021, **15**, 10542; K. M. Wyss, R. D. D. Kleine, R. L. Couvreur, A. Kiziltas, D. F. Mielewski and J. M. Tour, *Commun. Eng.*, 2022, **1**, 1; K. M. Wyss, W. Chen, J. L. Beckham, P. E. Savas and J. M. Tour, *ACS Nano*, 2022, **16**, 7804.
39 Y. Wang, Y. Shao, D. W. Matson, J. Li and Y. Lin, *ACS Nano*, 2010, **4**, 1790.
40 X. H. Hu, R. Zhang, Z. Wu and S. Xiong, *ACS Omega*, 2022, **7**, 27263.
41 P. Kokmat, P. Surinlert and A. Ruammaitree, *ACS Omega*, 2023, **8**, 4010.
42 H. Khojasteh, M. S. Niasari, H. Safajou and H. S. Hojaghan, *Diamond Relat. Mater.*, 2017, **79**, 133.
43 A. Suryawanshi, M. Biswal, D. Mhamane, R. Gokhale, S. Patil, D. Guin and S. Ogale, *Nanoscale*, 2014, **6**, 11664.